New Journal of Physics
The open access journal at the forefront of physics

Deutsche Physikalische Gesellschaft DPG IOP Institute of Physics

PAPER • OPEN ACCESS

The TRAPSENSOR facility: an open-ring 7 tesla Penning trap for laser-based precision experiments

To cite this article: Manuel J Gutiérrez *et al* 2019 *New J. Phys.* **21** 023023

New Journal of Physics
The open access journal at the forefront of physics

Deutsche Physikalische Gesellschaft DPG
IOP Institute of Physics

Published in partnership with: Deutsche Physikalische Gesellschaft and the Institute of Physics

OPEN ACCESS

RECEIVED
9 July 2018

REVISED
21 November 2018

ACCEPTED FOR PUBLICATION
20 December 2018

PUBLISHED
28 February 2019

PAPER

The TRAPSENSOR facility: an open-ring 7 tesla Penning trap for laser-based precision experiments

Manuel J Gutiérrez[1], Joaquín Berrocal[1], Juan M Cornejo[1,9], Francisco Domínguez[1], Jesús J Del Pozo[1], Iñigo Arrazola[2], Javier Bañuelos[1], Pablo Escobedo[1,10], Oliver Kaleja[3,4], Lucas Lamata[2], Raúl A Rica[1,5,11], Stefan Schmidt[1,12], Michael Block[3,4,6], Enrique Solano[2,7,8] and Daniel Rodríguez[1,5]

[1] Departamento de Física Atómica, Molecular y Nuclear, Universidad de Granada, E-18071, Granada, Spain
[2] Department of Physical Chemistry, University of the Basque Country UPV/EHU, Apartado 644, E-48080, Bilbao, Spain
[3] Institut für Kernchemie, Johannes Gutenberg-Universität Mainz, D-55099, Mainz, Germany
[4] GSI Helmholtzzentrum für Schwerionenforschung GmbH, D-64291, Darmstadt, Germany
[5] Centro de Investigación en Tecnologías de la Información y las Comunicaciones, Universidad de Granada, E-18071, Granada, Spain
[6] Helmholtz-Institut Mainz, D-55099, Mainz, Germany
[7] IKERBASQUE, Basque Foundation for Science, Maria Diaz de Haro 3, E-48013, Bilbao, Spain
[8] Department of Physics, Shanghai University, 200444 Shanghai, People's Republic of China
[9] Present address: Institut für Quantenoptik, Leibniz Universität Hannover, Welfengarten 1, D-30167, Hannover, Germany
[10] Present address: Departamento de Electrónica y Tecnología de Computadores, Universidad de Granada, E-18071, Granada, Spain
[11] Present address: Departamento de Física Aplicada, Universidad de Granada, E-18071, Granada, Spain
[12] Present address: Institut für Physik, Johannes Gutenberg-Universität Mainz, D-55099, Mainz, Germany

E-mail: danielrodriguez@ugr.es

Keywords: Penning trap, mass spectrometry, fluorescence detection, laser cooling, beam preparation

Abstract

A Penning-trap facility for high-precision mass spectrometry based on a novel detection method has been built. This method consists in measuring motional frequencies of singly-charged ions trapped in strong magnetic fields through the fluorescence photons from laser-cooled $^{40}Ca^{+}$ ions, to overcome limitations faced in electronic single-ion detection techniques. The key element of this facility is an open-ring Penning trap coupled upstream to a preparation Penning trap similar to those used at Radioactive Ion Beam facilities. Here we present a full characterization of the trap and demonstrate motional frequency measurements of trapped ions stored by applying external radiofrequency fields in resonance with the ions' eigenmotions, in combination with time-of-flight identification. The infrastructure developed to observe the fluorescence photons from $^{40}Ca^{+}$, comprising the 12 laser beams and the optical system to register the image in a high-sensitive CCD sensor, has been proved by taking images of the trapped and cooled $^{40}Ca^{+}$ ions. This demonstrates the functionality of the proposed laser-based mass-spectrometry technique, providing a unique platform for precision experiments with implications in different fields of physics.

1. Introduction

Mass measurements with the highest precision, on stable and exotic nuclei, are performed using Penning traps, outstanding and versatile tools for studying fundamental properties of atoms and ions [1, 2]. The required relative mass uncertainty $\delta m/m$ differs by several orders of magnitude depending on the area of application within physics, ranging from $\leqslant 10^{-7}$ for astrophysics and nuclear structure physics, to below 10^{-11} for contributions to neutrino mass measurements [2]. In order to fulfill the demand for higher sensitivity for heavy ions and to improve accuracy for specific studies, a variety of new precision Penning-trap mass spectrometers based on non-destructive detection schemes are at present under commissioning. For example, the PENTATRAP experiment at the Max Planck Institute for Nuclear Physics in Heidelberg has been built to perform ultra-high accuracy mass measurements on highly-charged heavy ions [3]. There is also a Penning-traps beamline coupled to the TRIGA reactor in Mainz [4], and a new Penning-trap system at GSI-Darmstadt,

which is part of an upgrade of the SHIPTRAP facility for precision measurements on superheavy elements (SHEs) [5].

Nowadays, two detection methods are utilized for precision mass measurements at Radioactive Ion Beam (RIB) facilities: the Time-of-Flight Ion-Cyclotron-Resonance (TOF-ICR) technique, or any of its variants [6, 7], and the Phase-Imaging Ion-Cyclotron-Resonance (PI-ICR) technique [8]. The TOF-ICR technique has been used for several decades, yielding relative mass uncertainties between 10^{-8} and 10^{-9}. The PI-ICR technique is a novel method and, by tracking the ion motion using a high-resolution position-sensitive micro-channel plate (MCP) detector, provides a five-fold gain in precision and a 40-fold increase in resolving power. Despite the outcomes obtained by means of these techniques (see e.g. [9] for TOF-ICR, and [10] for PI-ICR), both methods are limited in sensitivity since several tens of ions are needed to obtain a precise motional frequency value. This limits the applicability to the SHEs ($Z \geqslant 104$) produced in fusion-evaporation reactions with very low production yields, sometimes only of one ion per day or below. The atomic ion with the lowest production yield measured in a Penning trap is $^{256}Lr^{++}$ using the TOF-ICR method [11]. With the PI-ICR technique one could measure a few heavier elements (lower yields) since this method requires a smaller number of ions. However, for the rarest elements a technique requiring only one ion is mandatory. A well-known technique able to realize this purpose relies on the resonant pick-up of the current a single oscillating ion induces on the trap electrodes. This induced-image current technique, which has been used for ultra-precise cyclotron frequency measurements of ions with low or medium mass-to-charge ratios, and of fundamental particles [12–17], has not been demonstrated yet with ions with large mass-to-charge ratios.

Besides the on-going developments of a variant of the induced-image current technique for SHEs [5, 18], a novel method for mass spectrometry was proposed based on the use of a single laser-cooled $^{40}Ca^{+}$ ion as detector [19], following a scheme based on two traps described earlier [20]. In the first ever attempt to experimentally realize this concept, the sensitivity of a single $^{40}Ca^{+}$ ion laser-cooled to the Doppler limit ($T_{\text{limit}} \sim 1$ mK) has been characterized by studying its axial motion in an open-ring Paul trap [21, 22]. The analytical method and a first approach of using just one trap to store the ion of interest and the laser-cooled ion simultaneously has been recently presented [23], following a former idea described in [24]. Such scheme might allow identifying SHEs elements, after thermalization, transport and capture in a Penning trap with open-ring geometry [21], through the fluorescence photons emitted by the $^{40}Ca^{+}$ ion. The identification relies on the determination of motional frequencies, limiting the relative mass uncertainty $\delta m/m$ in the ion of interest to how precisely one can determine those frequencies from the fluorescence photons. Since the ion of interest is sympathetically cooled by Coulomb interaction with the $^{40}Ca^{+}$ ion, it will be possible to perform precision spectroscopy on a single trapped and cooled ion, extending the applicability of the technique used in [25], to the scenario where the single ion of interest is well under control in a high-intense and homogeneous magnetic field. Extending such laser spectroscopic techniques to rare isotopes of transuranium elements will open new perspectives for precision measurements of their nuclear properties. For example, isotope shift measurements could provide information on the differential charge radii in a nuclear model-independent way. Compared to in-gas cell spectroscopy techniques, a reduced Doppler broadening will result in higher precision. Furthermore, experiments can be conducted in the quantum-limited regime by using quantum-logic spectroscopy in a Penning trap like proposed in [26]. This will allow improving the control of such kind of experiment compared to the use of a linear Paul trap as an ion container [27], where the ion species have to be within a certain mass range and the radiofrequency prevents long coherence times.

The open-ring geometry of the Penning trap described in this article differs from all the traps built for precision and accurate mass spectrometry, which are made either by a stack of cylindrical electrodes, see e.g. [3, 28], or with electrodes with the shape of truncated hyperboloids of revolution, as for example the ones described in [29, 30]. In this publication the full facility around the open-ring Penning trap is described with special emphasis on the performance of this trap, presenting the first fluorescence measurements and proving Doppler cooling in the strongest magnetic field.

2. Experimental setup: the Penning-traps beamline

In a Penning trap, the ions are confined by the superposition of a homogeneous, strong magnetic field $\vec{B} = B\hat{z}$ and a quadrupolar electrostatic field created by the electrodes,

$$V(r, z) = \frac{qU}{2d^2}\left(z^2 - \frac{1}{2}r^2\right), \tag{1}$$

where q is the ion's charge, U the trapping potential and d the trap's characteristic distance (see e.g. [1] for more details). The motion of an ion stored in the trap can be depicted as the superposition of three independent modes. The motion along the axial direction, independent of the magnetic field, is a harmonic oscillation with

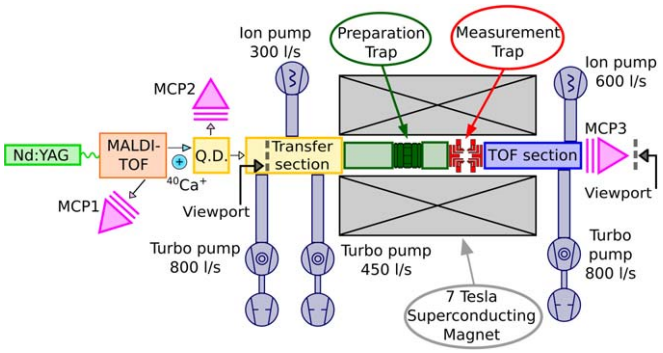

Figure 1. Schematic view of the Penning-traps beamline at the TRAPSENSOR laboratory. A view port was placed in the transfer section for the fluorescence measurements, decoupling the MALDI-TOF from the Penning traps. MCP3 is movable in and out of the beamline, for time-of-flight identification and fluorescence measurements, respectively.

amplitude ρ_z and frequency

$$\nu_z = \frac{1}{2\pi}\sqrt{\frac{U}{d^2}\frac{q}{m}}. \tag{2}$$

The other two motional degrees of freedom are in the radial plane, and they are referred to as reduced-cyclotron and magnetron motion, with radii represented by ρ_+ and ρ_-, respectively, and characteristic frequencies given by

$$\nu_\pm = \frac{\nu_c}{2}\left(1 \pm \sqrt{1 - 2\left(\frac{\nu_z}{\nu_c}\right)^2}\right). \tag{3}$$

ν_c is the free cyclotron frequency of the trapped ion,

$$\nu_c = \frac{1}{2\pi}\frac{q}{m}B, \tag{4}$$

which relates directly with the mass-to-charge ratio of the observable frequency. Thus, this is the quantity to be measured in order to determine the ion's mass. To achieve this, one can utilize the relationship

$$\nu_c = \nu_+ + \nu_-. \tag{5}$$

In a real Penning trap the electric field is not perfectly quadrupolar, having higher order components:

$$V(r, z) = C_2\left(z^2 - \frac{1}{2}r^2\right) + C_4\left(z^4 - 3r^2z^2 + \frac{3}{8}r^4\right) + \ldots. \tag{6}$$

In that case (or if there is a small tilt between electric and magnetic fields) equation (5) no longer holds and the frequency ν_c can then be unfolded from the so-called *invariance theorem* [1]

$$\nu_c^2 = \nu_+^2 + \nu_z^2 + \nu_-^2. \tag{7}$$

Measurements on ions produced at RIB facilities usually suffer from poor beam quality, for example a large kinetic-energy spread. Then, more instrumentation has to be added to the Penning trap in order to stop the ions, to cool and bunch them, and to separate the ion of interest from other ions species also present in the beam but often in rates several orders of magnitude larger.

Figure 1 shows a sketch of the TRAPSENSOR Penning-traps beamline built at the University of Granada for laser-based precision experiments. The facility comprises a laser-desorption ion source, a transfer section, two Penning traps, one for preparation, including isobaric separation, and one for the measurements, followed by a time-of-flight section. In the following, we describe in detail each of these elements.

2.1. Ion production and detection

Ions are produced outside the Penning traps by means of a laser-desorption ion source or inside one of the Penning traps via photoionization of an atomic calcium beam. For the fluorescence measurements and the commissioning tests of the setup solely $^{40}Ca^+$ ions were used.

The laser-desorption ion source is a commercial apparatus from Bruker Analytical Systems, Model Reflex III, originally designed for Matrix-Assisted Laser-Desorption-and-Ionization and Time-Of-Flight (MALDI-TOF) identification, to analyze large molecular samples. The source was tested and characterized delivering calcium, osmium and rhenium ions produced at kinetic energies ranging from 20 keV (nominal energy of the

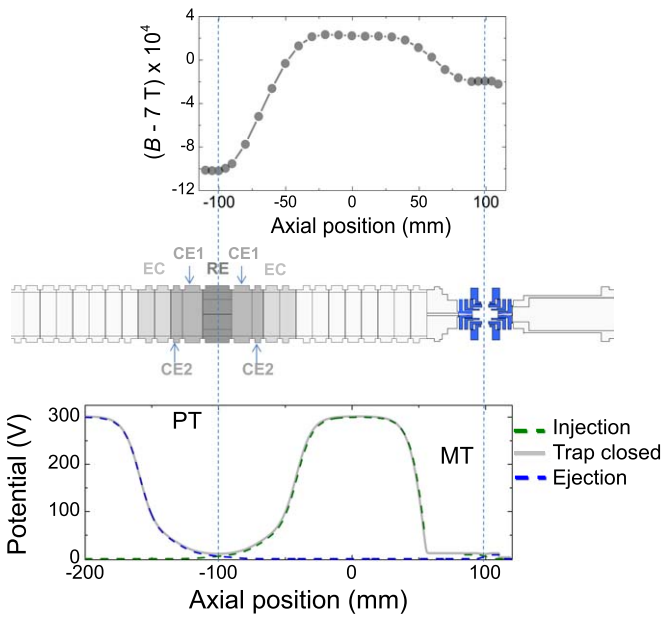

Figure 2. Longitudinal view of the Penning traps (center) showing the magnetic field strength (top) and the potentials along the z-axis for injection, capture and extraction (bottom). The acronyms PT and MT stand for Preparation and Measurement Trap, respectively. The electrodes in the center of the PT, i.e. EC (endcap), CE1,2 (correction electrodes) and RE (ring electrode) allow realizing a quadrupolar potential. The potentials of the MT are shown in figure 5.

apparatus), down to about 100 eV [31]. For the experiments presented here, the kinetic energy of the ions was fixed to 270 eV. The repetition rate of the frequency-doubled Nd:YAG laser ($\lambda = 532$ nm) is 10 Hz, with a pulse length of 4 ns and energies up to 75 mJ. The ion source is coupled to the beamline as shown schematically in figure 1. The transfer section is made of an electrostatic quadrupole deflector, two steerers and 16 electrostatic lenses.

Ions are detected and identified by their time-of-flight using one of the several MCP detectors located at different positions along the beamline: MCP1, MCP2 and MCP3 (figure 1). The MCP3 detector allows performing measurements of the eigenfrequencies as well as of ν_c of the ions stored in any of the Penning traps after they are ejected towards the detector.

2.2. The Penning-traps system

The Penning-traps system comprises two Penning traps housed in the same superconducting solenoid (figure 2). The superconducting solenoid has the same specifications as those in operation at SHIPTRAP [28], JYFLTRAP [32], MLLTRAP [33] and TRIGATRAP [4]. The first trap downstream from the transfer section is made of a stack of 27 cylinders following the conceptual design of the preparation Penning trap for MATS at FAIR [34], so as to allow performing buffer-gas cooling [35] or electron cooling [36]. A longitudinal view of the trap tower together with the magnetic field strength and the potential shape along the z-axis, for injection, trapping (and manipulation), and ejection is shown in figure 2. The center of the trap (dark-green area in figure 1) is located in the first homogeneous region of the superconducting solenoid with a magnetic field homogeneity of 10 ppm over 1 cm^3. The trap is closed with a potential barrier of 300 V when the ions are delivered with 270 eV kinetic energy. The ring electrode (RE) is eight-fold segmented to allow applying dipolar and quadrupolar fields to determine ν_+, ν_z, ν_- and ν_c. The second trap is an open-ring Penning trap [21, 37, 38], located in a region with a magnetic field homogeneity of 0.14(10) ppm over the volume of 1 cm^3. This trap, colored in blue and named MT in figure 2, is used for the measurements. It is described in detail in section 3. For the measurements presented here, the pressure values at both sides of the superconducting solenoid, close to the 800 l s^{-1} turbo pumps shown in figure 1, were around 10^{-8} mbar without using the ion pumps. When these were turned on (during laser cooling experiments) the pressure gauge in the ion pumps displayed 4×10^{-10} mbar in the Transfer section and 7×10^{-10} mbar in the TOF section. The latter reading improved to 5×10^{-11} mbar when using a liquid nitrogen cryopanel installed in the ion pump.

The PT was designed to allow cooling ions via collisions with gas atoms, but also to implement other cooling mechanisms compatible with ultra-high vacuum, since the pumping barrier between the traps (with a length of 23 mm and a diameter of 2 mm), limits the pressure difference between the PT and the MT. Thus, buffer-gas cooling in the PT restricts those experiments based on creating a two-ion crystal in the MT as envisaged [23]. However, cooling of ions in the PT should be possible by their interaction with a bath of electrons trapped at

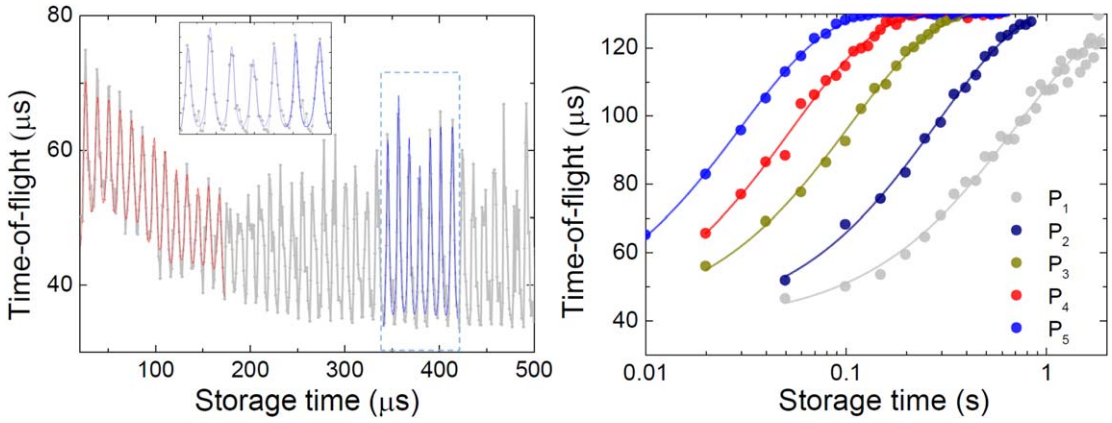

Figure 3. Left panel: Time-of-flight of $^{40}Ca^{+}$ ions from the PT to MCP3 (see figure 1) versus storage time in the PT for times below 500 μs. One of the correction electrodes at the injection side of the trap was connected to a circuit for induced current detection, and is polarized through a low-pass filter. The filter causes the rise time during ion capture to be slower for that correction electrode, and is thus responsible for the higher time-of-flight for storage times below 100 μs. The blue and red solid-lines are the results from multi-peak fits. Right panel: Time-of-flight of $^{40}Ca^{+}$ ions from the PT to MCP3 (see figure 1) as a function of the storage time in the PT for different buffer-gas pressures. The solid lines represent fits using the exponential grow function of equation (9). The pressure values inside the PT are obtained from the fit yielding $p_1 = 1.3 \times 10^{-6}$ mbar ($\tau_z^{\rm cool} \approx 700$ ms), $p_2 = 3.0 \times 10^{-6}$ mbar ($\tau_z^{\rm cool} \approx 300$ ms), $p_3 = 8.3 \times 10^{-6}$ mbar ($\tau_z^{\rm cool} \approx 100$ ms), $p_4 = 1.7 \times 10^{-5}$ mbar ($\tau_z^{\rm cool} \approx 50$ ms), and $p_5 = 2.9 \times 10^{-5}$ mbar ($\tau_z^{\rm cool} \approx 30$ ms).

Table 1. Eigenfrequencies for $^{40}Ca^{+}$ when the PT (figure 2) is operated with $V_{\rm EC} = 300$ V, $V_{\rm CE1} = 45$ V, $V_{\rm CE2} = 29.5$ V, and $V_{\rm RE} = 5$ V. (*) This value was obtained using the measured values of ν_c, and $\nu_\pm$ together with equation (7).

ν_+ (MHz)	ν_z (kHz)	ν_- (Hz)
2.688 592(2)	49.500(140)*	456(7)

room temperature in a nested trap [36], or with a cloud of laser-cooled ions. Sympathetic cooling with laser-cooled ions was proved in a Penning trap first on ions created inside the trap [39, 40]. Only very recently it was demonstrated in a Paul trap [41] and in a Penning trap [42] on externally created highly-charged ions. The second case is more relevant to the mass measurements of SHEs using fluorescence monitoring techniques, since they are produced externally with high kinetic energies.

The ions stored in the harmonic potential of the trap with axial frequency $\omega_z = 2\pi\nu_z$ experience a friction force of the form $\vec{F} = -2m\delta_z\vec{v}$, where m is the ions' mass and $\vec{v}$ their velocity. The cooling rate $\gamma_z = 2\delta_z$ of the ions' kinetic energy along the z-direction is determined by

$$\delta_z = \frac{q}{2m}\frac{1}{\mu_0}\frac{p_b/p_0}{T_b/T_0}, \tag{8}$$

with the ion mobility μ_0, the normalized residual gas pressure p_b/p_0 and the normalized buffer-gas temperature T_b/T_0. p_0 and T_0 are 1013 mbar and 293 K, respectively. The thermal ion mobility of singly-charged $^{40}Ca^{+}$ ions in a helium buffer-gas is considered equal to that of Ar^{+} ions such that $\mu_0 = 21.2 \times 10^{-4}\,m^2\,s^{-1}\,V^{-1}$ [43]. The corresponding cooling time constant is $\tau_z^{\rm cool} = 1/\gamma_z$. Figure 3 shows the time-of-flight of $^{40}Ca^{+}$ ions ejected from the PT towards the detector MCP3, as a function of the storage time. In the left panel one can see oscillations in the time-of-flight spectrum, depicting the axial oscillation of the ions in the PT during the first 500 μs of the cooling process. The axial oscillation frequency of the $^{40}Ca^{+}$ ions within this process varies from $\nu_z = 40.9(3)$ kHz, within the first hundred microseconds, to $\nu_z = 43.6(2)$ kHz for a storage time around 500 μs, and eventually $\nu_z = 49.50(14)$ kHz when the ions reach equilibrium with the buffer gas (calculated from the radial frequencies in table 1). The observed shift is due to the very large initial oscillation amplitudes (starting at 15 cm when the ions are injected). The radial eigenfrequencies were measured by probing the ions' motion in the radial direction with external dipolar fields varying $\nu_{\rm RF}$ around $\nu_\pm$.

The effect of the buffer-gas pressure on the cooling time is shown in the right panel of figure 3. The data points are fitted using the storage-time dependent function given by

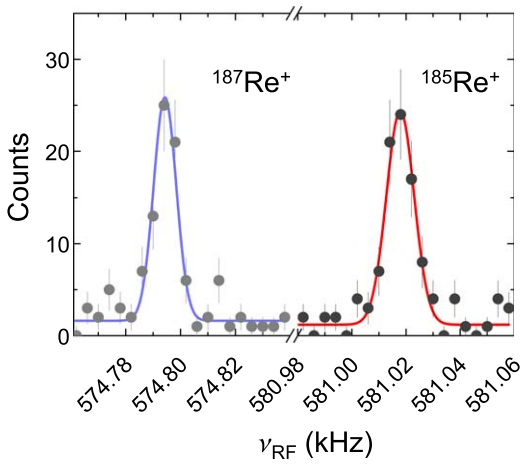

Figure 4. Cooling resonances in the PT for $^{185,187}Re^{+}$ ions. The resolving power $m/\Delta m$ is 5.7 × 10^4 and 4.8 × 10^4 for $^{187}Re^{+}$ and $^{185}Re^{+}$, respectively.

Table 2. Cyclotron frequency (ν_c) and resolving power ($m/\Delta m$) from cooling resonances in the PT.

Ion species	ν_c (Hz)	$m/\Delta m$
$^{40}Ca^{+}$	2689 067.5(3)	2.7 × 10^5
$^{185}Re^{+}$	581 017.9(7)	4.8 × 10^4
$^{187}Re^{+}$	574 794.5(5)	5.7 × 10^4

$$S(t) = S_M - (S_M - S_m)e^{-t/\tau_z^{cool}}, \tag{9}$$

where S represents here the average time-of-flight signal, and the subscripts M and m stand for the maximum and the minimum time-of-flight values, respectively. The helium buffer-gas pressure inside the PT is obtained from τ_z^{cool} using equation (8).

In case of the radial motions $\omega_{\pm}$the damping constants read

$$\delta_{\pm} = \pm 2\delta_z \frac{\omega_{\pm}}{\omega_+ - \omega_-}. \tag{10}$$

Thus, for a pressure of 1.3 × 10^{-6} mbar ($\tau_z^{cool} \approx$ 700 ms), $\delta_z \approx 0.7\,s^{-1}$, $\delta_+ \approx 1.4\,s^{-1}$, and $\delta_- \approx -2.4 \times 10^{-4}\,s^{-1}$. This yields a decay time constant for the magnetron motion of $\tau_-^{heat} \approx$ 4100 s, and thus, the increase of the magnetron radius within the storage time of the ions inside the PT is negligible. Note that the magnetron radius grows over time (minus sign in equation (10)), instead of shrinking, because of the collisions with the buffer gas atoms; thus, collisions *heat* the magnetron motion instead of cooling it.

The main purpose of the PT, which is centering the ions with specific mass-to-charge ratio to allow removing unwanted species, was tested using $^{40}Ca^{+}$ and $^{185,187}Re^{+}$ ions. The performance of the device with respect to the buffer-gas cooling technique [35] was described in [44, 45]. The centering of the ions with a specific mass-to-charge ratio is accomplished by combining the collisions with buffer-gas atoms with the application of an external quadrupolar field in the radial direction at $\nu_{RF} = \nu_c$. Figure 4 shows cooling resonances for the two naturally abundant rhenium isotopes, ^{185}Re and ^{187}Re. The frequencies for $^{40}Ca^{+}$ and $^{185,187}Re^{+}$ ions and the resulting resolving powers are listed in table 2. Comparing these frequencies with the one obtained for calcium and the literature value for their masses, the result is consistent within the expected precision, given the short excitation time.

The laser-desorption ion source delivers ions with 10 ns duration pulses directly into the PT every 100 ms. Since a measurement cycle might last up to several tens of seconds, stacking has been also implemented.

3. The open-ring Penning trap

The measurement Penning trap (MT) is an open-ring trap, shown in detail in figure 5, together with the trap potential along the z-axis for injection, trapping and ejection of the ions. The trap is made of two sets of four concentric rings forming the endcap electrodes (EC), the ring electrodes (REs), correction electrodes (CE) and

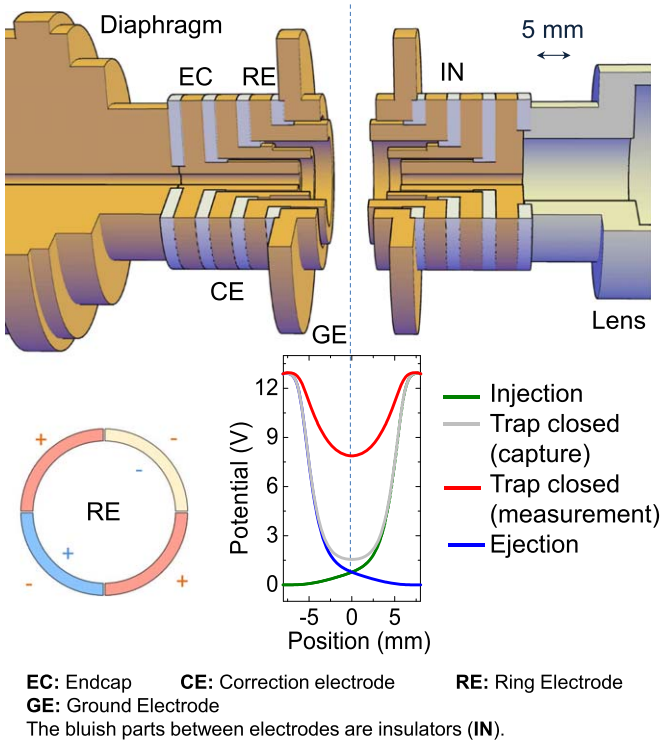

Figure 5. Three-dimensional CAD drawing of the open-ring Penning trap together with the potentials applied for injection, capture, measurement, and extraction. The RE is four-fold segmented to allow applying dipolar or quadrupolar RF excitations.

an external electrode, named grounded electrode (GE). The trap is located between the diaphragm, built after the PT, and the first electrostatic lens in the time-of-flight section. The REs are four-fold segmented in order to apply external radiofrequency fields with different polarities (dipolar and quadrupolar) in order to probe the eigenfrequencies of the ions and ν_c.

This geometry (figure 5) has never been used before in a Penning trap configuration. It was used previously in [21], introducing this trap for laser cooling experiments. The device was similar to the one built at GANIL (LPCTRAP) [46] for β–ν correlation experiments [47, 48] and in both cases operated as a Paul trap. The main advantage of this geometry is the absence of a conventional RE, which provides access in the radial plane without modifications, as opposed to cylindrical and hyperbolical traps, where holes would be necessary, compromising the revolution symmetry of the electric field. This makes it an ideal candidate for laser-based experiments with trapped ions, without compromising the trap performance, i.e. the trap can be used to perform traditional mass spectrometry experiments (TOF-ICR resonances) as will be shown in the following. However, there are also some difficulties arising from its use, namely the tuning (see appendix A) and the assembly, since having two halves without mechanical connection can lead to misalignments if the support structure is not carefully designed. The Penning trap presented here (figure 5) has been scaled down by a factor of 2 with respect to the Paul trap variants [21–23, 46, 48] and an additional electrode has been added.

3.1. Trap performance

The performance of the trap has been investigated from measurements of ν_+, ν_z, ν_-, and ν_c, and simulations of the time-of-flight signal of $^{40}Ca^+$ ions from the MT to the MCP3 through the TOF section. The average time-of-flight of the ions from the center of the MT (z_{MT}) to the detector MCP3 (z_{det}) is given by [6]

$$S = \int_{z_{MT}}^{z_{det}} \sqrt{\frac{m}{2(E_z - qU(z) + |\mu(E_r^{kin})B(z)|)}}\, dz, \tag{11}$$

where E_z is the total initial axial energy, $E_r^{kin}(t)$ is the radial kinetic energy and $U(z)$ and $B(z)$ are the electric potential and magnetic field strength along the z-axis, respectively. The ion's orbital magnetic moment μ is given by

$$|\mu| = |\pi \cdot q \cdot (\rho_+^2 \nu_+ + \rho_-^2 \nu_-)| = \left| \frac{E_r^{kin}}{B_0} \right|, \tag{12}$$

where B_0 is the magnetic field intensity at the trap's center.

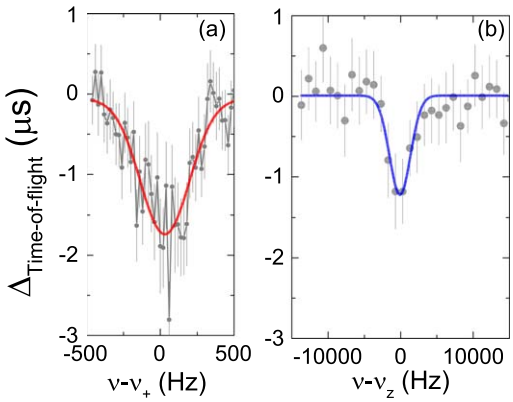

Figure 6. (a) Determination of the reduced-cyclotron frequency of $^{40}Ca^+$ ions in the open-ring trap. (b) Determination of the axial frequency (equation (2)) of $^{40}Ca^+$ ions in the open-ring trap. The excitation time was 100 ms.

Table 3. Eigenfrequencies for $^{40}Ca^+$, determined by measuring the time-of-flight of the ions from the MT to the MCP3 detector, after probing the eigenmotions with an external dipolar field (figure 6). The MT (figure 5) is operated with $V_{EC} = 13$ V, $V_{RE} = 5.8$ V, and $V_{GE} = 0$ V. The table also lists the values of Ud^2 obtained from ν_+ (equation (13)) and ν_z (equation (2)).

V_{CE} (V)	ν_+ (MHz)	U/d^2 V mm^{-2}	ν_z (kHz)	U/d^2 V mm^{-2}
9.82	2.685 203(11)	0.3667(12)	149.916(93)	0.3674(5)
10.14	2.685 135(17)	0.3727(18)	150.277(231)	0.3692(11)
10.42	2.685 090(27)	0.377(3)	152.109(679)	0.378(4)

Figure 6(a) shows a measurement of the reduced-cyclotron frequency obtained by applying an external dipolar field at ν_+ via the RE segments. In the absence of any external RF excitation field, the mean time-of-flight of the extracted $^{40}Ca^+$ ions from the MT to the MCP3 detector is 75.5(1) μs, which corresponds to an initial ions' mean kinetic energy of 2.08(6) eV. This is the outcome after comparing the experimental results with those obtained from SIMION simulations by implementing the MT together with the lenses in the time-of-flight section, the MCP3 detector and the magnetic field gradient. Furthermore, using a different voltage configuration during the ejection of the ions, the initial mean kinetic energy is also ≈2.1 eV, for a measured average time-of-flight of 78.9(3) μs. From cooling measurements in the MT, performed in similar way as those shown in figure 3, the ions are thermalized in the trap, so this energy might be gained in the extraction process, or there could be a time-of-flight offset arising from the signal processing and/or the acquisition system. Assuming this energy is only axial energy, the radius of the reduced-cyclotron orbit the ions would have to yield the minimum time-of-flights in figure 6(a) is $\rho_+ \approx 250$ μm (left). The time-of-flight effect after probing the axial motion is shown in figure 6(b). The mean kinetic energy of the ions is 3.8 eV. However, since the initial energy is biased, the energy originated from the external field is 1.7 eV, corresponding to a maximum axial oscillation amplitude $\rho_z = 4.6$ mm.

The eigenfrequencies of $^{40}Ca^+$ ions are shown in table 3. The voltage applied to the CE was chosen to minimize C_4 (see appendix A) when $V_{EC} = 13$ V. These frequencies are obtained from the time-of-flight of the ions from the MT to the detector after probing their eigenmotions. From the measured values of ν_+ and ν_z, it is possible to obtain the ratio U/d^2 from equation (2) and

$$\nu_+ = \frac{qB}{2\pi m} - \frac{U}{4\pi d^2 B}, \tag{13}$$

obtained by expanding equation (3) to second order in ν_z/ν_c.

For the measurement of ν_z, it is necessary to drive the axial motion of the ions to large amplitudes, so some frequency shift is expected. This frequency shift depends on C_4 (see equation (6)) as

$$\Delta\nu_z = \frac{3qC_4E_{\text{axial}}}{8\pi^2 m^2 \nu_z^3}, \tag{14}$$

with $E_{\text{axial}} = 1.7$ eV. This can be used to estimate C_4 by comparing the experimentally determined frequency with the one obtained from the simulations by substituting C_2^{sim} in equation (2). This can be compared to

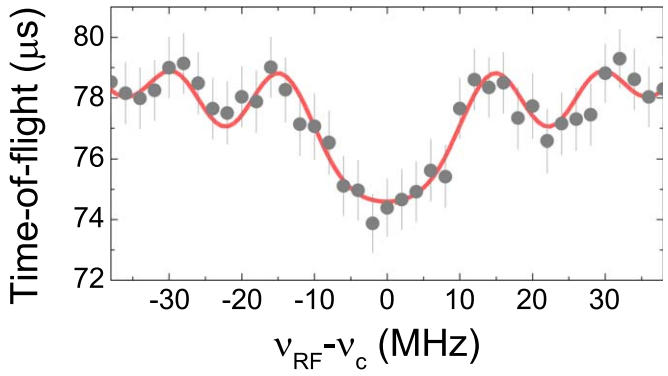

Figure 7. Time-Of-Flight Ion-Cyclotron-Resonance for $^{40}Ca^{+}$ ions. The voltage configuration was Config. 1 (table 4). ν_c is the cyclotron frequency. See text for further details.

Table 4. MT cyclotron frequency measurements for $^{40}Ca^{+}$ for different voltage configurations (Config.). $V_{CE} = 9.82$ V and $V_{GE} = 13$ V in Configuration 1, and $V_{CE} = 10.14$ V and $V_{GE} = 0$ V in Configuration 2. $V_{EC} = 13$ V, and $V_{RE} = 5.8$ V in both configurations. The values of ν_c (TOF-ICR) are the mean values from seven measurements. The uncertainties correspond to 1 σ. ($^{\#}$) $\nu_z = 146.918(208)$ kHz was obtained using $2\nu_+\nu_- = \nu_z^2$, and the measured values of $\nu_+ = 2.685\,360(7)$ MHz and $\nu_- = 4019(6)$ Hz.

Config.	ν_c (TOF-ICR) (MHz)	ν_c (equation (7)) (MHz)	ν_c (equation (5)) (MHz)
1	2.689 3743(7)	2.689 379(19)$^{\#}$	2.689 379(13)
2	2.689 3723(9)	2.689 340(30)	2.689 428(35)

the C_4^{sim} obtained by fitting the potential along the z-axis, to check that they are of the same order. More precise determinations are not possible, since the fitting routine is limiting the precision of C_2^{sim} and C_4^{sim}.

3.2. Cyclotron-frequency measurements

The mass-to-charge ratio of an ion is determined from its cyclotron frequency using equation (4), where the magnetic-field strength B is measured via the cyclotron frequency of a reference ion with a precisely known mass value (see e.g. [2]). In turn, ν_c can be unfolded from the measurements of the eigenfrequencies of the ions using equation (7), or by applying an external quadrupolar radiofrequency field that will originate energy exchange between the radial eigenmodes (see equation (5)). Scanning the radiofrequency ν_{RF} around ν_c and measuring, for each frequency value, the time-of-flight of the ions from the MT to the detector, results in a TOF-ICR measurement [6], similar to the one shown in figure 7 for $^{40}Ca^{+}$ ions. In this case, a radiofrequency field with an amplitude $V_{RF} = 76$ mV $_{pp}$ was applied for a time T_{RF}= 100 ms. This amplitude drives five conversions between magnetron and reduced-cyclotron motion. More TOF-ICR measurements using $^{40}Ca^{+}$ ions have been taken for $T_{RF} = 50$, 100 and 200 ms. The maximum mass resolving power obtained for $^{40}Ca^{+}$ from the TOF-ICR measurements is $m/\Delta m = 6.6 \times 10^5$. A single TOF-ICR measurement was taken to determine ν_c for $^{187}Re^{+}$, yielding 574.8861(25) kHz ($T_{RF} = 25$ ms and $m/\Delta m = 1.8 \times 10^4$). This result is in good agreement with the measured calcium frequencies within the expected precision, for this excitation time.

Equation (7) is utilized to obtain ν_c when the eigenfrequencies are measured using a non-destructive detection technique, i.e. detecting the current induced by a stored ion in the trap electrodes (e.g. [12]) or, as envisaged in our future experiments, using fluorescence photons from a laser-cooled $^{40}Ca^{+}$ ion [19]. However, in this publication we have measured the eigenfrequencies via time-of-flight, after applying an external dipolar field. The three cyclotron-frequency values obtained from the eigenfrequencies listed in table (3), are 2.689 388 (16), 2.689 340(30), and 2.689 342(65) MHz, which are in agreement with $\nu_c = 2.689\,373(3)$ MHz, resulting from 30 measurements carried out by means of the TOF-ICR technique [6], during a period of six months, after performing the regular B_0-dump maintenance of the magnet. For these measurements, several voltage configurations were adopted yielding a standard deviation in ν_c of ≈2.7 Hz, and thus ensuring the harmonicity of the field. The relative fluctuations of the magnetic field have been recently measured during 1 h, obtaining $\delta B/B = 1.9 \times 10^{-7}$.

Table 5. Absolute frequencies of optical transitions of the $^{40}Ca^{+}$ ion. The saturation intensity I_0 is 433 μW mm^{-2} for $^2S_{1/2} \rightarrow {}^2P_{1/2}$ transition and 3.4 and 3.3 μW mm^{-2}, for the transitions $^2D_{3/2} \rightarrow {}^2P_{1/2}$, and $^2D_{5/2} \rightarrow {}^2P_{3/2}$, respectively. Γ is the decay rate (or linewidth) of the transition. (*) This value is obtained from the frequency values of the $^2S_{1/2} \rightarrow {}^2P_{3/2}$ and $^2S_{1/2} \rightarrow {}^2D_{5/2}$ transitions quoted in [52, 53].

Atomic Transition	Frequency (MHz)	$\Gamma/2\pi$ (MHz)
$^2S_{1/2} \rightarrow {}^2P_{1/2}$	755 222 766.2(1.7) [54]	21.57(8) [55]
$^2D_{3/2} \rightarrow {}^2P_{1/2}$	346 000 234.867(96) [56]	1.482(8) [55]
$^2D_{5/2} \rightarrow {}^2P_{3/2}$	350 862 882.830(91) [57]*	1.350(6) [58]

4. Fluorescence measurements: Doppler cooling in 7 tesla

The main scientific goal of the TRAPSENSOR Penning-traps facility is to use a single laser-cooled $^{40}Ca^{+}$ ion as high-sensitive sensor for precision Penning-trap mass spectrometry [19]. The characterization of a single laser-cooled $^{40}Ca^{+}$ ion was accomplished using a Paul trap [22], including the scenario with two ions in the trap [23]. The technique exploits the eigenmodes of a two-ion crystal, and the relationship between the eigenfrequencies and the ions' masses, to obtain the mass of the target ion. From the technical point of view, moving the experiment from a Paul-trap platform to another one based on a 7 T Penning trap complicates considerably the setup due to the Zeeman effect on the $^{40}Ca^{+}$ atomic transitions and the complex image collection system. A detailed description of the gain in sensitivity and precision using the single laser-cooled $^{40}Ca^{+}$ ion in a 7 tesla Penning trap will be presented elsewhere.

Laser cooling of $^{40}Ca^{+}$ in a Penning trap was achieved earlier in a magnetic field of 1 T [49], and more recently, by the same group, in 1.86 T [50]. Increasing the magnetic field to 7 T complicates laser cooling significantly. The second order Zeeman splitting, which is asymmetrical and scales with $\sim B^2$, demands a more complex laser scheme to address all the transitions. The high magnetic field and the large dimensions of the superconducting solenoid force the image collection system to be very long (about 2 m), which poses a challenge in terms of image quality and efficiency.

4.1. Level scheme, frequency stabilization and laser beam transport

$^{40}Ca^{+}$ is alkali-like, and thus it has a single valence electron in the $4^2S_{1/2}$ ground state. The first excited state is the $4^2P_{1/2}$-state, which decays with a probability of 12/13 back into the ground state (at $\lambda = 397$ nm) and with 1/13 into the meta-stable $3^2D_{3/2}$-state (at $\lambda = 866$ nm). In the presence of a magnetic field $\vec{B}$, due to j-mixing, there is a non-zero probability that the electron decays into the $3^2D_{5/2}$-state, with a branching ratio given by $4.2 \times 10^{-7} B^2\,\mathrm{T}^{-2}$ [51]. The population can be unshelved using the $4^2P_{3/2}$-state (at $\lambda = 854$ nm). The absolute frequencies for these transitions in the absence of magnetic field are listed in table 5.

In the presence of an external magnetic field B the energy levels are no longer degenerated due to Zeeman effect. The resulting level scheme, with calculations up to second-order perturbation theory, is shown in figure 8.

The experimental laser arrangement for Doppler cooling comprises eight lasers with wavelengths 397 nm ($\times 2$), 866 nm ($\times 4$) and 854 nm ($\times 2$). The lasers are regulated by means of an ultra-accurate wavemeter with an absolute accuracy of 10 MHz. The lasers and control system as well as the outcomes from the regulation have been shown in previous works, i.e. in [59] and [60]. The sketch of the setup to generate the sidebands from the two carrier frequencies around the wavelength of 854 nm using an Electro Optical Modulator was presented in [61]. The laser beams are combined using standard optics elements, optical fibers, and they are all linearly polarized before entering the vacuum beamline.

Figure 9 shows a three-dimensional cut drawing of part of the Penning-traps tower with the PT and the MT, indicating the axial laser beams for Doppler cooling. The figure shows the support structure made of MACOR, where three calcium ovens are placed. The laser beams for photoionization at $\lambda = 422$ and 375 nm, are also indicated in the figure. The resonant transition $^1S_0 \rightarrow {}^1P_1$ ($\Delta m_j = +1$) has been used (422 nm). The frequency for this transition is 98 GHz above the value used in the Paul trap experiments [22], due to the confinement of the ion in the 7 tesla magnetic field.

4.2. Fluorescence detection and Doppler cooling

The fluorescence photons from the $4^2S_{1/2} \rightarrow 4^2P_{1/2}$ transition in $^{40}Ca^{+}$ are registered by an Electron Multiplying Charge-Coupled Device (EMCCD) located approximately two meters downstream from the center of the open-ring trap. The sensor of the camera has 1024 $\times$ 1024 pixels, with a pixel size of 13 μm $\times$ 13 μm, thus having an active area

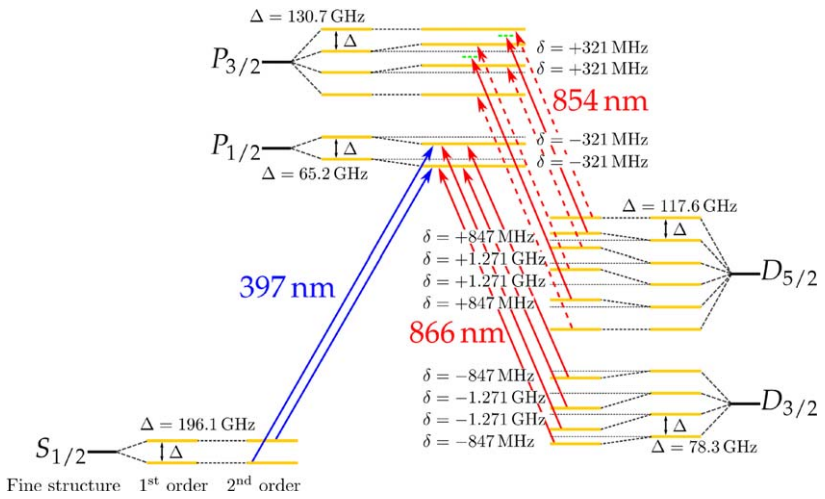

Figure 8. Atomic level scheme of $^{40}Ca^{+}$ in a 7 T magnetic field. The figure shows the relevant transitions to perform Doppler cooling. First and second order effects of the magnetic field are included. The solid arrows represent the transitions driven by single lasers, while the dashed arrows represent transitions generated from lasers after using and Electro Optical Modulator. For the $D_{5/2}$ pumping, two of the driving beams (the ones pumped by the main 854 nm laser beams) have an additional detuning when the sidebands are on resonance. This relative detuning is equal to +52 MHz.

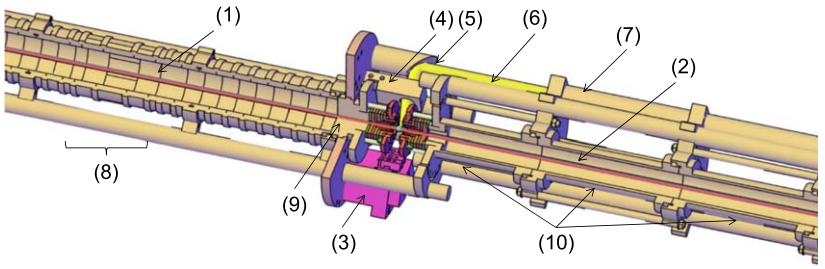

Figure 9. Three-dimensional cut drawing showing part of the Penning-traps tower, together with the laser beams: (1) photoionization laser beams (crossing the MT from left to right), (2) laser beams for Doppler cooling (crossing the MT from right to left), (3) support structure for calcium ovens, (4) support structure holding the first lens of the image collection system ($f = 25$ mm), (5) mirror of the image collection system, (6) surface depicting the size of the collimated fluorescence photons, (7) part of the structure housing the lenses inside vacuum, (8) PT, (9) diaphragm, and (10) electrostatic lenses of the time-of-flight section for identification.

of 13.3 × 13.3 mm^2. The optical system comprises a mirror, seven lenses (six of them inside vacuum, placed along 1.5 m), and an objective with variable magnification. The positions of the first lens and the mirror are indicated in figure 9. The first lens has a focal distance of 25 mm and subtends a solid angle of about 1.6 %. The set of all the lenses provides a fixed magnification factor, which combined with the objective might yield a further magnification by a factor of 12. Figure 10 shows images from the fluorescence photons emitted by a $^{40}Ca^{+}$ ion cloud interacting with the 12 laser beams. The $^{40}Ca^{+}$ ions are produced via photoionization inside the MT. In the first series of measurements the influence of each of the eight lasers (12 beams) has been observed, as well as the effect of the photoionization lasers.

The maximum fluorescence signal has been obtained when the 397 nm lasers are detuned −20 MHz below resonance, and the detuning for all the infrared lasers is $\Delta = -30$ MHz (see figure 10). This detuning has been optimized later to about −10 and −20 MHz for the 397 nm and infrared lasers, respectively, (near resonance keeping in mind that the absolute accuracy of the wavemeter is 10 MHz). The fluorescence signal decreases for larger detuning of the 397 nm lasers, as observed when shifting the laser frequencies between −100 and −300 MHz. In the images shown in figures 10(a) and (b), the centers of the ion clouds obtained from the two-dimensional Gaussian fits given in pixels are (34.6,18.6) and (37.1,21.8), respectively. This allows measuring the magnification factor from the displacement of the trap center (figure 10(d)), resulting in 3.2(5) when the variable magnification of the objective was set to the lowest value. The fluorescence distributions are different, resulting in $\sigma_z \sim 250$ μm and $\sigma_r \sim 320$ μm for the symmetric configuration (a), and $\sigma_z \sim 305$ μm and $\sigma_r \sim 355$ μm for the non-symmetric one (b). The rotation of the ion cloud with respect to the EMCCD (see figure 10) has to be accounted for when calculating the cloud size in the axial and radial directions.

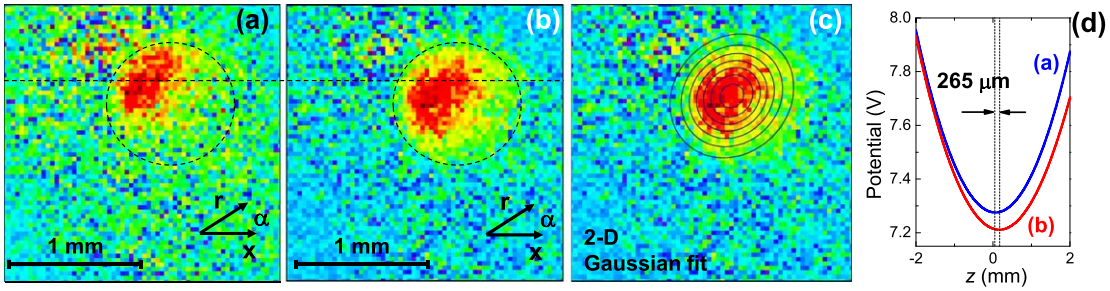

Figure 10. Images of the fluorescence photons from a $^{40}Ca^{+}$ ion cloud formed and stored in the 7 tesla open-ring Penning trap. The detunings of the lasers were fixed to $\Delta_{397-\mathrm{nm}} = -20$ MHz and $\Delta_{\mathrm{infrared}} = -30$ MHz. (a) and (b) differs in the potential applied to the endcap electrodes; in (a) the potential configuration is symmetric and in (b) non-symmetric. The two potential shapes along the axial direction are shown in (d) where the displacement of the trap center can be observed. The corresponding displacement between the images can be visualized following the dashed line and circumferences in (a) and (b). The acquisition time was 5 s, and each pixel in these images correspond to 16 × 16 pixels of the sensor. The plot labeled (c) shows a two-dimenional Gaussian fit to the image (b).

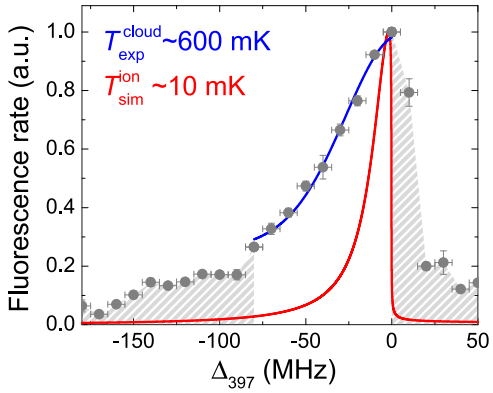

Figure 11. Fluorescence rate (gray circles) recorded as a function of the frequency detuning of the cooling lasers ($S_{1/2} \rightarrow P_{1/2}$). The infrared lasers were fixed. The laser powers are given in appendix B. Each data point is the average of three measurements. For each of these measurements the full cycle was repeated. i.e. the ions are created, laser-cooled and ejected. The blue-solid line is the Voigt fit of those experimental data points where laser cooling is clearly observed. Following equation (15) and the results from the fit, the temperature of the cooled ion cloud is $T \sim 600(100)$ mK. The red-solid line is the result from simulating the laser cooling of one ion using the model described in appendix C. The extracted temperature is 10 mK. The experimental data and the results from simulations were normalized to their respective maxima.

Doppler cooling has been reached for ion clouds. The area of the fluorescence image is reduced by a factor of 5 within 1 s (time step in the EMCCD) of interaction between the laser beams and the initially hot ions. The 397 nm lasers are close to resonance and the infrared lasers are detuned −20 MHz. Figure 11 shows the measured fluorescence rate as a function of the frequency detuning of the 397 nm lasers. The figure also shows the result from simulating the cooling of a single ion, using the model described in appendix C. Only part of the experimental data are fitted using a Voigt function. The width of the Lorentzian distribution is fixed to the cooling transition's width (see table 5). The temperature of the cooled ion cloud (T) is obtained from the width of the Gaussian distribution $\Delta\nu(G)$ (in turn from the Voigt fit) using the equation [21, 49]

$$T = \frac{mc^2}{8k_{\mathrm{B}}\ln 2}\left|\frac{\Delta\nu(G)}{\nu_0}\right|^2, \tag{15}$$

where ν_0 is the frequency of the transition and k_{B} is the Boltzmann's constant. The shaded data points have been discarded because the shrinkage of the cloud is not clearly seen for these laser frequencies. Counts are also observed above resonance due to the size of the cloud. If all data points with negative detuning are considered, the temperature is 900(110) mK.

While cooling has clearly been achieved, there are issues preventing the laser-cooled ions from staying in the trap for long times. From the measured time-of-flight spectra, $^{40}CaO^{+}$ and heavier ions with $m \sim 240$ amu appear in the spectrum besides $^{40}Ca^{+}$. The ratio between contaminant ions and $^{40}Ca^{+}$ increases with the storage time in the MT. All these ions are formed in reactions, with residual atoms or molecules, since the $^{40}Ca^{+}$ ions are created resonantly. The vacuum is currently under improvement in order to minimize the presence of contaminants in the trap.

5. Conclusions and outlook

At the University of Granada, we have built a full Penning-traps beamline setup to perform precision experiments using different ion species, in similar way as it is done at existing Penning-traps systems coupled to RIB facilities worldwide [4, 28–30, 32–34]. In addition, the TRAPSENSOR facility has two outstanding features, i.e. (1) the novel geometry of the open-ring 7 tesla Penning trap, which has been characterized in detail in this publication using established detection techniques, and (2) the lasers and fluorescence-image collection systems, built around the traps tower, to carry out laser spectroscopy. Moreover, for the first time laser-cooling experiments have been carried out in a 7 T field. This is beneficial to perform single-ion Penning trap mass spectrometry using a single laser-cooled ion as detector.

Our ion choice to perform the first laser-cooling experiments is $^{40}Ca^{+}$, since it has no hyperfine structure and it is relatively heavy compared to other ions species that can be laser cooled. It needs twelve laser beams due to the large energy splitting arising from the Zeeman effect (first and second order). This does not occur in the other Penning-trap experiments of the same nature. Among six Penning-trap experiments in the world performing laser cooling on positive ion species, only one at the Imperial College in London is using $^{40}Ca^{+}$ ions ($B = 1.86$ tesla) [50]. One experiment uses $^{25}Mg^{+}$ at GSI-Darmstadt ($B = 4.1$ tesla) [62], and four experiments use $^{9}Be^{+}$ ions; at NIST-Boulder ($B = 4.45$ tesla) [63], and at the Universities of Hannover ($B = 5$ tesla) [26], Mainz ($B = 1.95$ tesla) [64] and Sydney ($B \sim 2$ tesla) [65]. In this publication, we have shown the first fluorescence measurement (photons with $\lambda = 397$ nm), proving the interaction of the ions with the laser-cooling beams. Furthermore we have shown Doppler cooling. This constitutes an important step towards the Doppler-cooling of a single $^{40}Ca^{+}$ ion. Its subsequent application as a high-sensitive sensor will enable precision experiments in the framework of nuclear and fundamental physics. Reaching the quantum regime, by performing ground-state cooling in 7 tesla would only require one extra laser with $\lambda = 729$ nm, thus not introducing more complexity compared to such kinds of experiments in $B = 1.86$ tesla [66]. The implementation of such cooling mechanism will be also interesting in the field of quantum technologies, for example for digital-analog quantum simulations of spin models as Heisenberg [67], or spin-boson models as the Dicke model, in a variety of coupling regimes and inhomogeneities.

Acknowledgments

This work was supported by the European Research Council (contract no. 278648-TRAPSENSOR), from the Spanish MINECO/ FEDER (project nos. FPA2012-32076, FPA2015-67694-P, FIS2015-69983-P, UNGR10-1E-501, UNGR13-1E-1830), Ramón y Cajal Grant RYC-2012-11391, Juan de la Cierva grant IJCI-2015-26091, Centro Nacional de Partículas, Astropartículas y Nuclear CPAN13-TM01, and 'Sistema Nacional de Garantía Juvenil y del Programa Operativo de Empleo Juvenil'; from the Spanish MECD (PhD grant nos. FPU15-04679 and FPU17/02596); from Junta de Andalucía/FEDER (project no. IE-57131) and 'Programa de Empleo Juvenil; from Basque Government (PhD grant no. PRE-2015-1-0394) and (project no. IT986-16), and from the University of Granada 'Plan propio-Programa de Intensificación de la Investigación PP2017-PRI.I-04'. I.A, L.L. and E.S acknowledge also support from projects OpenSuperQ (820363) and QMiCS (820505) of the EU Flagship on Quantum Technologies. We warmly thank Klaus Wendt for arranging the loan of the MALDI-TOF apparatus from the University of Mainz to the University of Granada.

Appendix A. Trap tuning

The Penning trap presented here has been scaled down by a factor of 2 with respect to the Paul trap variant [21–23, 46, 48]. The quadrupolarity of the potential has been investigated through SIMION simulations [68] for different voltage configurations in order to minimize the coefficient C_4 (equation (6)). The potential along the z-axis is recorded and fitted using equation (6). Figure A1 shows $|C_4|$ as a function of the voltage applied to the CE V_{CE}, for three different values of V_{EC}. For all the data points $V_{RE} = 5.8$ V and $V_{GE} = 0$ V. A similar procedure was followed (the results are not shown) keeping a constant value of V_{EC}, equal to 13 V. In this case, C_4 was calculated as a function of V_{CE} for three different values of V_{RE}, namely, 1.8, 3.8, and 5.8 V. V_{GE} was set to 0 V. From the results obtained using SIMION, C_4 can be minimized by taking

$$V_{CE} = 0.655(3) \cdot V_{EC} + 1.63(4), \tag{A.1}$$

or $V_{CE} = 0.273\,6(11) \cdot V_{RE} + 8.552(4)$, when tuning the trap by varying the voltage applied to the RE as a function of V_{EC} or V_{RE}, respectively. ν_z is obtained for each configuration from the coefficient C_2. For the voltages applied, ν_z was varied from about 100 to 200 kHz. Using again the results from the SIMION simulations (keeping $V_{RE} = 5.8$ V), it is possible to build the polynomial function

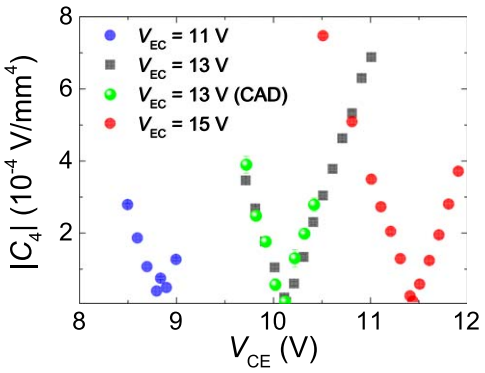

Figure A1. Absolute value of the coefficient C_4 as a function of the voltage applied to the correction electrode (V_{CE}). The data points are obtained after fitting with the function made out of the first two terms in equation (6), the potential shape along the z-axis obtained from SIMION simulations. For this purpose the CAD file shown in figure 5 was converted to a SIMION . PA# file using SL Tools.

$$\frac{V_{EC}}{V_{CE}} = A_0 + A_1\nu_z + A_2\nu_z^2, \tag{A.2}$$

with $A_0 = 0.873(21)$, $A_1 = 0.004\,0(3)\,\mathrm{kHz}^{-1}$, and $A_2 = -8(1) \times 10^{-6}\,\mathrm{kHz}^{-2}$. Deciding on an axial frequency, the voltages to be applied at EC and CE are obtained by solving the system formed by equations (A.1) and (A.2). This allows tuning the trap close to the final value of the experiment. Note that the power supply (model BS1-8 from Stahl Electronics) delivers signals in the range $\pm 15.000(1)$ V. By changing V_{EC} and V_{CE}, the bottom of the potential along the MT is biased from 6 to 9 V, so that the ions can be captured using the scheme shown in figure 5.

Appendix B. Frequencies of the cooling transitions for $^{40}Ca^+$ in 7 tesla

The calculated transition frequencies for this work's magnetic field are presented in table B1. First and second order perturbation theory corrections for the Zeeman effect have been taken into account. The latter caused shifts up to ~1.2 GHz (see figure 8). All lasers used in the experiment are *External Cavity Diode Lasers* DL100/ Pro from TOPTICA.

Table B1. Absolute frequencies of the transitions of the $^{40}Ca^{+}$ ion and the ^{40}Ca atom in a magnetic field $B = 6.998\,747$ T. The third column shows the standard deviations from the fixed frequency values during the laser frequencies' regulation process. All laser beams are collimated with a diameter of ∼2 mm at the trap's center. The laser powers were measured after they pass through the traps. For the 397 nm lasers the power was 1.6 and 7.9 mW for $\Delta m = -1$ and $\Delta m = +1$, respectively. For the infrared lasers the values were 1 − 2 mW. (*) The 854 nm lasers are set to a frequency ∼50 MHz above the resonant value, so that the sidebands hit the desired transitions on-resonance.

Atomic transition	ν_{laser} (MHz)	σ_{laser} (MHz)
$^2S_{1/2} \rightarrow {}^2P_{1/2}$		
$m_j = -1/2 \rightarrow m_j = +1/2$	755 353 131	1.17(1)
$m_j = +1/2 \rightarrow m_j = -1/2$	755 091 763	3.78(2)
$^2D_{3/2} \rightarrow {}^2P_{1/2}$		
$m_j = -3/2 \rightarrow m_j = -1/2$	346 085 624	0.511(3)
$m_j = -1/2 \rightarrow m_j = +1/2$	346 072 955	0.349(1)
$m_j = +1/2 \rightarrow m_j = -1/2$	345 929 407	0.297(1)
$m_j = +3/2 \rightarrow m_j = +1/2$	345 915 894	0.328(1)
$^2D_{5/2} \rightarrow {}^2P_{3/2}$		
$m_j = -5/2 \rightarrow m_j = -3/2$	350 960 839	(Sideband)
$m_j = -3/2 \rightarrow m_j = -1/2$	350 973 405*	0.363(1)
$m_j = -1/2 \rightarrow m_j = +1/2$	350 986 075	(Sideband)
$m_j = +1/2 \rightarrow m_j = -1/2$	350 737 798	(Sideband)
$m_j = +3/2 \rightarrow m_j = +1/2$	350 751 310*	0.443(2)
$m_j = +5/2 \rightarrow m_j = +3/2$	350 764 926	(Sideband)
$^1S_0 \rightarrow {}^1P_1$ (atom)		
$m_j = 0 \rightarrow m_j = +1$	709 176 380	(Not regulated)
$^1P_1 \rightarrow$ continuum (atom)	∼799 450 000	(Not tuneable)

Appendix C. Doppler cooling model

Several simulations have been carried out to study the optimal settings to search for Doppler cooling. The simulations use the model from [62], which in turn builds upon the laser cooling model presented in [69], considering additionally the effects of the residual gas present in the trap. A brief overview will be presented here.

All the equations in the model consider only adimensional quantities. Thus, the energies are scaled by $E_0 = \hbar\Gamma\sqrt{1+s_0}/2$ and the times by $t_0 = 2(1+s_0)/(\Gamma s_0)$, where $s_0 = I/I_0$ is the saturation parameter. The relevant quantities are then

$$\epsilon = \frac{E}{E_0}, \qquad \delta = \frac{\hbar\Delta}{E_0}, \qquad r = \frac{E_R}{E_0}, \qquad \text{and} \qquad \tau = \frac{t}{t_0}, \tag{C.1}$$

where E is the ion's kinetic energy, Δ is the detuning of the cooling laser and $E_R = (\hbar k_z)^2/2m$ is the recoil energy of the ion when a photon is emitted. k_z is here the linear momentum of the cooling laser's photons.

Introducing $Z = i\Big/\sqrt{1-(\delta+i)^2/4\epsilon r}$, the rate equation for the ion's energy is [62]

$$\frac{d\epsilon}{d\tau} = -2\delta_z(\epsilon - \epsilon_m) + \frac{4}{3}r\frac{1}{2\sqrt{\epsilon r}}\,\mathrm{Im}\,(Z) + \frac{1}{2\sqrt{\epsilon r}}[\mathrm{Re}\,(Z) + \delta\,\mathrm{Im}\,(Z)]. \tag{C.2}$$

Here, the first term accounts for the effects of the residual gas, and the second and third terms describe the effects of the ion-laser interaction. ϵ_m is the minimum energy attainable by buffer-gas cooling, and δ_z was defined in equation (8).

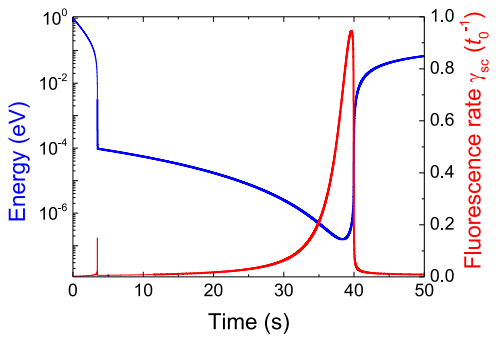

Figure C1. Doppler cooling of $^{40}Ca^{+}$ ions in helium buffer gas at 300 K. The background pressure was $\sim 10^{-7}$ mbar, and for this calculation only the $4^2S_{1/2} \rightarrow 4^2P_{1/2}$ has been considered ($\Gamma/2\pi = 21.57(8)$ MHz). The saturation parameter s_0 was 0.4.

The scaled fluorescence rate, in turn, is given by [62]

$$\gamma_{sc} = \frac{dN_{ph}}{d\tau} = \frac{1}{2\sqrt{\epsilon r}} \mathrm{Im}\,(Z). \tag{C.3}$$

Figure C1 shows the evolution of the ion's energy (left axis) and fluorescence rate (right axis) as a function of time, obtained by solving equations (C.2) and (C.3). For this figure only the cooling transition in $^{40}Ca^{+}$ ($^2S_{1/2} \rightarrow {}^2P_{1/2}$) has been considered, i.e., assuming a two-level system (like in the case of $^{24}Mg^{+}$ [62]). However, this transition is not closed for $^{40}Ca^{+}$, where the population will have to be repumped from additional levels. The saturation parameters and detunings of these repumping drivings will affect the cooling rate in a non-trivial manner, and a more complete model will be needed to fully understand their effect [70].

ORCID iDs

Manuel J Gutiérrez https://orcid.org/0000-0003-4115-6450
Joaquín Berrocal https://orcid.org/0000-0001-6816-0498
Francisco Domínguez https://orcid.org/0000-0002-5290-033X
Pablo Escobedo https://orcid.org/0000-0002-1701-8878
Lucas Lamata https://orcid.org/0000-0002-9504-8685
Raúl A Rica https://orcid.org/0000-0001-5308-9422
Daniel Rodríguez https://orcid.org/0000-0002-2989-7566

References

[1] Brown L S and Gabrielse G 1986 *Rev. Mod. Phys.* **58** 233–311
[2] Blaum K, Dilling J and Nörtershäuser W 2013 *Phys. Scr.* **2013** 014017
[3] Repp J *et al* 2012 *Appl. Phys.* B **107** 983–96
[4] Ketelaer J *et al* 2008 *Nucl. Instrum. Methods Phys. Res.* A **594** 162–77
[5] Giacoppo F *et al* 2017 *Acta Phys. Pol.* B **48** 423–9
[6] König M, Bollen G, Kluge H J, Otto T and Szerypo J 1995 *Int. J. Mass Spectrom. Ion Process.* **142** 95–116
[7] George S *et al* 2007 *Phys. Rev. Lett.* **98** 162501
[8] Eliseev S *et al* 2013 *Phys. Rev. Lett.* **110** 082501
[9] Block M *et al* 2010 *Nature* **463** 785–8
[10] Eliseev S *et al* 2015 *Phys. Rev. Lett.* **115** 062501
[11] Minaya Ramirez E *et al* 2012 *Science* **337** 1207–10
[12] Cornell E A, Weisskoff R M, Boyce K R, Flanagan R W, Lafyatis G P and Pritchard D E 1989 *Phys. Rev. Lett.* **63** 1674–7
[13] Häffner H *et al* 2003 *Eur. Phys. J.* D **22** 163–82
[14] Van Dyck R S, Pinegar D B, Van Liew S and Zafonte S L 2006 *Int. J. Mass Spectrom.* **251** 231–42
[15] Sturm S *et al* 2014 *Nature* **506** 467–70
[16] Ulmer S *et al* 2015 *Nature* **524** 196–9
[17] Heiße F *et al* 2017 *Phys. Rev. Lett.* **119** 033001
[18] Minaya Ramirez E *et al* 2013 *Nucl. Instrum. Methods Phys. Res.* B **317** 501–5
[19] Rodríguez D 2012 *Appl. Phys.* B **107** 1031–42
[20] Heinzen D J and Wineland D J 1990 *Phys. Rev.* A **42** 2977–94
[21] Cornejo J M, Colombano M, Doménech J, Block M, Delahaye P and Rodríguez D 2015 *Rev. Sci. Instrum.* **86** 103104
[22] Domínguez F, Arrazola I, Doménech J, Pedernales J S, Lamata L, Solano E and Rodríguez D 2017 *Sci. Rep.* **7** 8336
[23] Domínguez F *et al* 2018 *J. Mod. Opt.* **65** 613–21
[24] Drewsen M, Mortensen A, Martinussen R, Staanum P and Sørensen J L 2004 *Phys. Rev. Lett.* **93** 243201

[25] Laatiaoui M et al 2016 Nature 538 495–8
[26] Niemann M, Paschke A G, Dubielzig T, Ulmer S and Ospelkaus C 2014 CPT test with (anti)proton magnetic moments based on quantum logic cooling and readout CPT and Lorentz Symmetry-Proceedings of the Sixth Meeting vol 1 (Bloomington, IN: Indiana University Press) pp 41–4
[27] Schmidt P O, Rosenband T, Langer C, Itano W M, Bergquist J C and Wineland D J 2005 Science 309 749–52
[28] Block M et al (the SHIPTRAP Collaboration) 2005 Eur. Phys. J. A 25 49–50
[29] Mukherjee M et al 2008 Eur. Phys. J. A 35 1–29
[30] Ringle R, Bollen G, Prinke A, Savory J, Schury P, Schwarz S and Sun T 2009 Nucl. Instrum. Methods Phys. Res. A 604 536–47
[31] Cornejo J M, Lorenzo A, Renisch D, Block M, Düllmann C E and Rodríguez D 2013 Nucl. Instrum. Methods Phys. Res. B 317 522–7
[32] Kolhinen V S et al 2004 Nucl. Instrum. Methods Phys. Res. A 528 776–87
[33] Weber C, P Müller P and Thirolf P G 2013 Int. J. Mass Spectrom. 349-350 270–6 100 years of Mass Spectrometry
[34] Rodríguez D et al 2010 Eur. Phys. J. ST 183 1–123
[35] Savard G et al 1991 Phys. Lett. A 158 247–52
[36] Hall D S and Gabrielse G 1996 Phys. Rev. Lett. 77 1962–5
[37] Cornejo J M, Gutiérrez M J, Ruiz E, Bautista-Salvador A, Ospelkaus C, Stahl S and Rodríguez D 2016 Int. J. Mass Spectrom. 410 22–30
[38] Rica R A, Domínguez F, Gutiérrez M J, Bañuelos J, del Pozo J J and Rodríguez D 2018 Eur. Phys. J. ST 227 445–56
[39] Larson D J, Bergquist J C, Bollinger J J, Itano W M and Wineland D J 1986 Phys. Rev. Lett. 57 70–3
[40] van Eijkelenborg M A, Storkey M E M, Segal D M and Thompson R C 1999 Phys. Rev. A 60 3903–10
[41] Schmöger L et al 2015 Science 347 1233–6
[42] Schmidt S et al 2018 J. Mod. Opt. 65 538–48
[43] Ellis H W, Thackston M G, McDaniel E W and Mason E A 1984 At. Data Nucl. Data Tables 31 113–51
[44] Cornejo J M and Rodríguez D 2016 Nucl. Instrum. Methods Phys. Res. B 376 288–91
[45] Cornejo J M 2016 The preparation Penning trap and recent developments on high-performance ion detection for the project TRAPSENSOR PhD Thesis Universidad de Granada
[46] Rodríguez D et al 2006 Nucl. Instrum. Methods Phys. Res. A 565 876–89
[47] Fléchard X et al 2008 Phys. Rev. Lett. 101 212504
[48] Fléchard X et al 2011 J. Phys. G: Nucl. Part. Phys. 38 055101
[49] Koo K, Sudbery J, Segal D M and Thompson R C 2004 Phys. Rev. A 69 043402
[50] Mavadia S, Stutter G, Goodwin J F, Crick D R, Thompson R C and Segal D M 2014 Phys. Rev. A 89 032502
[51] Crick D R, Donnellan S, Segal D M and Thompson R C 2010 Phys. Rev. A 81 052503
[52] Wolf A L, van den Berg S A, Ubachs W and Eikema K S E 2009 Phys. Rev. Lett. 102 223901
[53] Guan H, Huang Y, Liu P L, Bian W, Shao H and Gao K L 2015 Chin. Phys. B 24 054213
[54] Wolf A L, van den Berg S A, Gohle C, Salumbides E J, Ubachs W and Eikema K S E 2008 Phys. Rev. A 78 032511
[55] Hettrich M, Ruster T, Kaufmann H, Roos C F, Schmiegelow C T, Schmidt-Kaler F and Poschinger U G 2015 Phys. Rev. Lett. 115 143003
[56] Gebert F, Wan Y, Wolf F, Angstmann C N, Berengut J C and Schmidt P O 2015 Phys. Rev. Lett. 115 053003
[57] König K, Geppert C, Krämer J, Maaß B, Otten E W, Ratajczyk T and Nörtershäuser W 2017 Hyperfine Interact. 238 24
[58] Gerritsma R, Kirchmair G, Zähringer F, Benhelm J, Blatt R and Roos C F 2008 Eur. Phys. J. D 50 13–9
[59] Cornejo J M, Escobedo P and Rodríguez D 2014 Hyperfine Interact. 227 223–37
[60] Escobedo P 2014 Desarrollo de un sistema de control para láseres de diodo utilizando moduladores acústico-ópticos Master's Thesis Universidad de Granada
[61] Gutiérrez M J 2016 Estudio de la fluorescencia de un ion de ^{40}Ca. en una trampa magnética de 7 T Master's Thesis Universidad de Granada
[62] Murböck T, Schmidt S, Birkl G, Nörtershäuser W, Thompson R C and Vogel M 2016 Phys. Rev. A 94 043410
[63] Gilmore K, Bohnet J, Sawyer B, Britton J and Bollinger J 2017 Phys. Rev. Lett. 118 263602
[64] Bohman M et al 2018 J. Mod. Opt. 65 568–76
[65] Ball H, Marciniak C, Wolf R, Hung A T H, Pyka K and Biercuk M 2018 arXiv:1807.00902
[66] Goodwin J, Stutter G, Thompson R and Segal D 2016 Phys. Rev. Lett. 116 143002
[67] Arrazola I, Pedernales J S, Lamata L and Solano E 2016 Sci. Rep. 6 30534
[68] SIMION® 8.0 Ion and Electron Optics Simulator https://simion.com/
[69] Wesenberg J H et al 2007 Phys. Rev. A 76 053416
[70] Janacek H A 2015 Optical Bloch equations for simulating trapped-ion qubits PhD Thesis University of Oxford